Geophysical Journal International

Geophys. J. Int. (2025) **240,** 1790–1801
Advance Access publication 2025 January 25
GJI Gravity, Geodesy and Tides

https://doi.org/10.1093/gji/ggae404

The 2023 M_w 6.9 Sarez, Tajikistan earthquake: subparallel faulting and distributed deformation of the Pamir

Xing Huang [1], Romain Jolivet [2,3], Yanchuan Li,[1] Xinjian Shan[1] and Bryan Raimbault [2,4]

[1] *State Key Laboratory of Earthquake Dynamics, Institute of Geology, China Earthquake Administration,* 100029 *Beijing, China. E-mail: xjshan@ies.ac.cn*
[2] *Laboratoire de Géologie, Département de Géosciences, UMR* 8538, *École normale supérieure-PSL,* 24 *rue Lhomond,* 75005 *Paris, France*
[3] *Institut Universitaire de France,* 1 *rue Descartes,* 75005 *Paris, France*
[4] *Univ. Grenoble Alpes, Univ. Savoie Mont Blanc, CNRS, IRD, Univ. Gustave Eiffel, ISTerre,* 38000 *Grenoble, France*

Accepted 2024 November 7. Received 2024 October 9; in original form 2024 May 7

SUMMARY

The central Pamir plateau moves northward and collides into Eurasia at a rate that varies significantly over its 600-km-wide extension. However, the active structures accounting for such internal shear strain remain enigmatic. In this study, we use Interferometric Synthetic Aperture Radar (InSAR) data to investigate the coseismic and post-seismic deformation of the M_w 6.9 Sarez earthquake on 23 February 2023. Using a Bayesian framework, we find the most likely seismogenic fault geometry and explore the full solution space of slip distributions. Our results highlight the main shock ruptures a nearly NNE fault dipping to the southeast. The finite-fault model exhibits a purely left-lateral strike-slip mechanism with little to no slip reaching the surface. Most of the coseismic slip remains confined to a depth of ∼5 to 20 km, consistent with a large shallow slip deficit. Post-seismic afterslip, which decays rapidly within the month following the main shock, cannot compensate for such coseismic shallow slip deficit. Integrating the analysis of coseismic slip, post-seismic deformation and regional seismic activity, we argue that in the central Pamir, significant north–south shear strain is accommodated along multiple parallel faults, often unmapped, hence posing a significant seismic hazard.

Key words: Satellite geodesy; Earthquake hazards; Earthquake source observations; Kinematics of crustal and mantle deformation.

1 INTRODUCTION

The Pamir plateau, located in the northwest of the Tibetan plateau, is formed of east–west trending belts formed during the late Palaeozoic and Mesozoic (Burtman & Molnar 1993; Schwab *et al.* 2004). Driven by the collision of the Indian Plate into Eurasia, Pamir moved northward over the last 25 Ma (Sobel *et al.* 2011) and thrusted over the Tajik depression (Fig. 1a). Such northward motion has been accommodated by the Chaman fault and the Darvaz fault to the west (Tapponnier *et al.* 1981; Burtman & Molnar 1993) and by the Karakorum and the Kashgar-Yecheng fault to the east (Cowgill 2010; Sobel *et al.* 2011). Currently, the Pamir plateau and the Tarim basin move northward with respect to stable Eurasia at a comparable rate, hence the dextral transpressive Kashgar-Yecheng fault separating Pamir from Tarim being mostly inactive (Cowgill 2010; Zubovich *et al.* 2010; Sobel *et al.* 2011). To the north, convergence between Pamir and Eurasia is mostly accommodated by the main Pamir thrust and the main Alai thrust, which absorb about 15 mm yr^{-1} as inferred from Global Navigation Satellite System (GNSS) campaigns (Mohadjer *et al.* 2010; Zubovich *et al.* 2010; Ischuk *et al.* 2013). Such shortening rates cause intense crustal seismicity along the main Pamir thrust, including, for instance, the 2016 M_w 6.4 Sary-Tash earthquake (Sippl *et al.* 2013; Schurr *et al.* 2014; Vajedian *et al.* 2017). Within the Pamir (Fig. 1b), the Sarez-Karakul (SK) fault system, which strikes NNE, accommodates left-lateral shear and east–west extension between the eastern and the western Pamir (Schurr *et al.* 2014). Several neotectonic structures and crustal earthquakes show the SK fault system is more active than the thrust fault systems within the Pamir, that is the Tanymas thrust system and the Sarez-Murghab thrust system (Schurr *et al.* 2014; Kulikova *et al.* 2016; Elliott *et al.* 2020; Bloch *et al.* 2021, 2023). Spatially, the SK fault system and its southwestward continuation into the Hindu Kush of Afghanistan are characterized by distributed deformation (Schurr *et al.* 2014). However, because of difficult field work conditions (mostly elevated topography), geological investigations are inherently difficult, limiting our in-depth understanding of the active geological structures in this region. In particular, active structures might not have been perfectly identified, and the

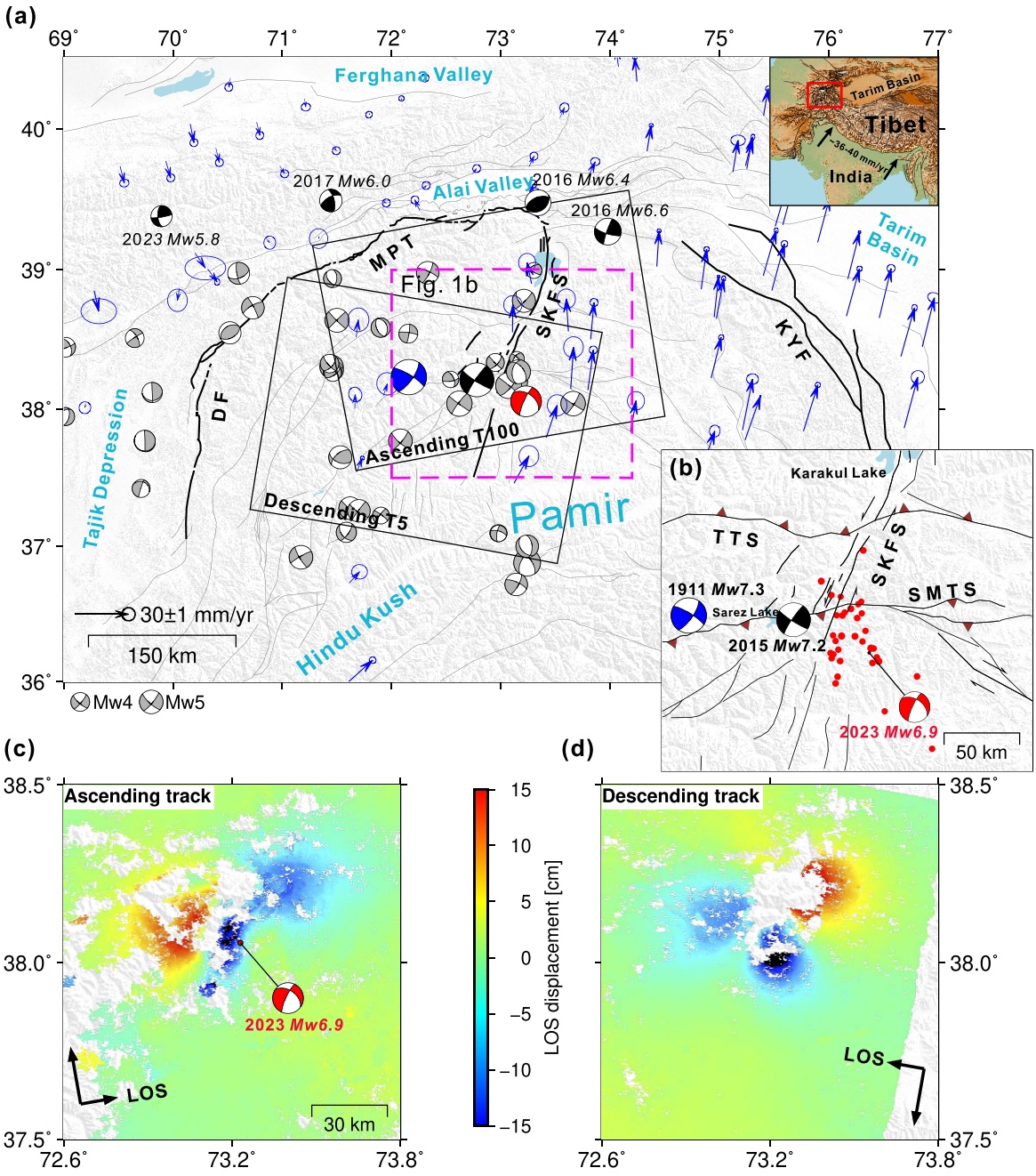

Figure 1. Regional tectonic setting of the Pamir plateau. (a) Black rectangles show the spatial coverage of the Sentinel-1 acquisitions along ascending (T100) and descending (T5) tracks. Blue arrows are interseismic GNSS velocities with respect to the stable Ferghana valley block. Error ellipses indicate the 70 per cent confidence level (Wang & Shen 2020). Grey focal mechanisms are from Schurr *et al.* (2014). The inset map shows the location of the Pamir region within the India–Eurasia collision zone. (b) Zoomed-in map of the central Pamir as indicated by the magenta dashed rectangle in (a). Red dots are aftershocks of the 2023 Sarez earthquake from USGS ($M > 4$, last accessed May 2023). Grey and black lines in (a) and (b) are mapped active faults in Pamir (Mohadjer *et al.* 2010). Blue focal mechanism of the 1911 M_w 7.3 Sarez-Pamir earthquake is from Kulikova *et al.* (2016). Red focal mechanism represents the 2023 M_w 6.9 Sarez earthquake. Black focal mechanisms ($M_w \geq 6.0$) indicate the locations of earthquakes that have occurred in the Pamir plateau since 2015 (e.g. the 2015 M_w 7.2 Murghab earthquake). Both black and red focal mechanisms are from USGS. SKFS: Sarez-Karakul fault system. MPT: Main Pamir Thrust. DF: Darvaz fault. KYF: Kashgar-Yecheng fault. TTS: Tanymas Thrust System. SMTS: Sarez-Murghab thrust system. The corrected coseismic deformation associated with the 2023 M_w 6.9 Sarez earthquake derived from ascending (c) and descending (d) tracks (Fig. S2). Positive values in (c) and (d) correspond to ground motion toward the satellite, and negative values denote ground motion away from the satellite.

corresponding seismic hazard and partitioning of the deformation remain quite enigmatic.

On 23 February 2023, a crustal earthquake with a moment magnitude of M_w 6.9 occurred in the Pamir, fortunately causing only a few damages. The hypocentre of the 2023 Sarez earthquake, as reported by the United States Geological Survey (USGS), is located at 38.055°N, 73.229°E, southeast of the Sarez Lake. The focal mechanism of the Sarez earthquake inferred from teleseismic data and from preliminary analysis of InSAR data indicates a dominantly strike-slip motion with a slight normal component,

consistent with the expected tectonic motion along the SK fault system (Shi *et al.* 2023; USGS 2023). In the same region, two significant earthquakes, including the 1911 M_w 7.3 Sarez-Pamir earthquake (Kulikova *et al.* 2016) and the 2015 M_w 7.2 Murghab earthquake (Sangha *et al.* 2017), have ruptured with comparable strike-slip mechanisms (Fig. 1b). While the epicentre of the 2015 Murghab earthquake is located right at the southern tip of the SK fault system, the latest models propose that the epicentre of the 1911 Sarez-Pamir earthquake is located ∼100 km to the west of the mapped SK fault system (Kulikova *et al.* 2016), raising the question of the focusing of strike-slip motion across the Pamir. The 2023 Sarez earthquake provides hence a good opportunity to study the seismogenic context and the kinematics of the area. This event also raises questions relating to a potential triggering relationship between the 2015 Murghab and the 2023 Sarez earthquakes.

We use Interferometric Synthetic Aperture Radar (InSAR) data to investigate the coseismic and early post-seismic surface motion associated with the 2023 Sarez earthquake. We first detail the coseismic and first 4 months of post-seismic surface deformation of this earthquake using Sentinel-1 observations. We then explore the optimal fault geometry and solve for the static coseismic and post-seismic slip distribution at depth using a fully Bayesian approach. We finally evaluate stress interactions between the 2015 Murghab and the 2023 Sarez earthquakes. Integrating the analysis of coseismic slip, post-seismic deformation and regional seismic activity, we discuss the associated kinematics in the central Pamir.

2 DATA AND METHODS

2.1 InSAR data and processing

We compute series of coseismic interferograms covering the main shock region using pre- and post-earthquake SAR images from ascending track 5 and descending track 100 (Fig. 1a and Table S1) using the TOPS module of the InSAR Scientific Computing Environment (Rosen *et al.* 2012). We correct for topographic phase contribution using the 1 arc-second Shuttle Radar Topography Mission (SRTM) digital elevation model (DEM, Farr *et al.* 2007) and remove the orbital phase contribution using precise orbit data from the Alaska Satellite Facility. We unwrap the interferometric phase on each interferogram using SNAPHU, a statistical minimum cost-flow approach (Chen & Zebker 2002). We mask pixels with a coherence lower than 0.3. Due to significant atmospheric phase delay influencing the ascending images, we enlarge the temporal baselines and process six interferograms (Fig. S1and Table S1). The relevant tropospheric effects contained by ascending and descending interferograms are mitigated using the GACOS software (Yu *et al.* 2017, 2018). We finally correct interferograms from a best-fitting bilinear ramp to remove long wavelength atmospheric perturbations and potential orbital inaccuracies (Wang & Fialko 2015; Yu *et al.* 2020). Final line-of-sight (LOS) displacements for the ascending (20 230 122–20 230 311) and descending (20 230 221–20 230 305) interferograms with good coherence are shown in Figs 1(c), (d) and S2. On the ascending track interferogram, we observe up to 15 cm of relative ground motion in the direction of the line-of-sight. Comparable ground motion in the opposite direction is observed on the descending track interferogram, confirming that ground motion is to first order horizontal and in agreement with the sinistral focal mechanism from USGS. We also observe a loss of coherence in the vicinity of the fault due to large displacement gradients and to the potential presence of snow in this winter season.

We detect and quantify potential early post-seismic deformation using acquisitions along the same SAR acquisition tracks. We measure surface post-seismic displacement using the same processing strategy as for the coseismic interferograms. Given the magnitude of the earthquake, we only expect detectable deformation in the days to weeks following the main shock. For simplicity, we do not reconstruct time series of motion but only evaluate ground displacement on individual interferograms. Since the azimuth of the descending track is approximatively parallel to the strike of the seismogenic fault, we only consider interferograms from acquisitions along the ascending track. Along this structure, we build a series of short profiles across the fault to evaluate potential shallow afterslip.

2.2 Geodetic slip inversions

Because the 2023 Sarez earthquake ruptured a previously unmapped fault, we first explore possible geometries for the seismogenic source, assuming uniform slip in a homogeneous elastic half-space (Okada 1985). We use the Markov Chain Monte Carlo approach, implemented in GBIS (Bagnardi & Hooper 2018) to extract the distribution of possible fault models explaining the InSAR data, an approach comparable to that of Shi *et al.* (2023). Effectively, we transition from an *a priori* Probability Density Function (PDF) to the *a posteriori* PDF informed by the InSAR data. We evaluate the possible fault parameters, including fault length, depth, width, strike, dip, and position. We also explore the slip values along this fault, assuming constant slip along the fault.

We then use the most probable fault geometry inferred with this method to solve for the detailed slip distribution of the 2023 M_w 6.9 Sarez earthquake at depth. From the location of the fault and its orientation, we extend it up to the surface, at depth and laterally. Our final fault plane is 60 km long and 30 km wide with a strike of 26° and a dip angle of 73° toward the east (Fig. 2 and Table S2). We discretize this fault plane with triangular elements using PyDistMesh, an adaptation of the original MATLAB implementation of DistMesh by Persson & Strang (2004). Triangular patches are smaller at shallow depths and larger at greater depths (Fig. S3; e.g. Jolivet *et al.* 2023). We define the forward model as $\boldsymbol{d}_{obs} = \boldsymbol{Gm}$, where $\boldsymbol{d}_{obs}$ is the LOS InSAR data, $\boldsymbol{m}$ is the vector of strike and dip slip values at each node of the triangular mesh and $\boldsymbol{G}$ is the Green's functions relating fault slip to surface displacement. Unlike the method used for inverting the seismogenic fault geometry in a homogeneous crustal model, here, we compute the Green's functions within a stratified elastic half-space based on the *P*- and *S*-wave velocity models in the central Pamir (Fig. S4; Mechie *et al.* 2012) using the EDKS software (Zhu & Rivera 2002). Effectively, slip on the fault is the linear interpolation between slip values at each node of the triangular fault mesh, and we build the Green's functions accordingly using the same approach as Jolivet *et al.* (2020). All fault models, Green's functions computation, data downsampling and model solution explorations are performed using the CSI software (https://github.com/jolivetr/csi, Jolivet *et al.* 2015).

Because of near fault decorrelation, we obtain less InSAR pixels near the fault trace (Figs 1c and d). Hence, any linear inversion method will poorly constraint at shallow depth, explaining potential differences in inferred finite-fault models (Huang *et al.* 2017). Recently, this was especially the case for the 2021 M_w 7.4 Maduo earthquake (e.g. Zhao *et al.* 2021; Chen *et al.* 2024a). Therefore,

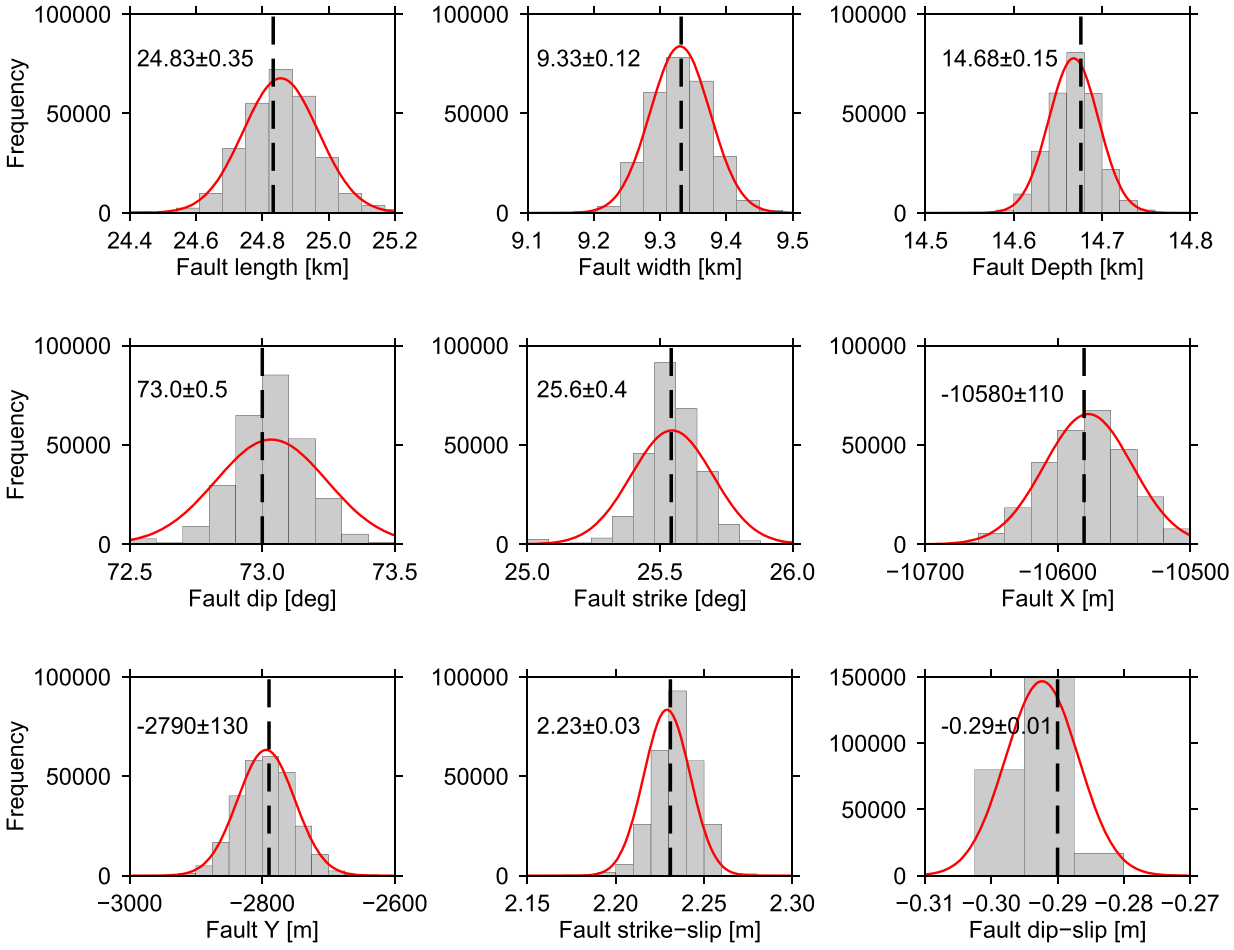

Figure 2. Marginal posterior probability distributions of source parameters of the 2023 M_w 6.9 Sarez earthquake. Black dashed lines in each subgraph represent the optimal solutions (Table S2).

in order to provide a quantitative estimate of the uncertainties associated with slip, and in particular at shallow depth, we explore the full space of slip solutions compatible with our InSAR data using a Bayesian approach (Minson *et al.* 2013; Jolivet *et al.* 2014, 2015). We define the posterior PDF of our coseismic slip model, $p(\boldsymbol{m}|\boldsymbol{d}_{\rm obs})$, as

$$p\left(\boldsymbol{m}|\boldsymbol{d}_{\rm obs}\right) \propto p\left(\boldsymbol{m}\right) \exp\left[-\frac{1}{2}(\boldsymbol{d}_{\rm obs}-\boldsymbol{G}\boldsymbol{m})^T \boldsymbol{C}_\chi^{-1}\left(\boldsymbol{d}_{\rm obs}-\boldsymbol{G}\boldsymbol{m}\right)\right]. \quad (1)$$

The prior PDF of the slip model, $p(\boldsymbol{m})$, is a description of our prior knowledge on the parameters of the model. We use uniform priors for strike-slip (between 0 and 8 m) and dip-slip (between −1 and 1 m). The misfit covariance matrix, $\boldsymbol{C}_\chi$, is the sum of the geodetic data covariance matrix $\boldsymbol{C}_d$, describing the errors in the data, and the prediction uncertainties matrix $\boldsymbol{C}_p$, accounting for uncertainties introduced by approximations of the forward model (Duputel *et al.* 2014). We assume that noise in the InSAR data far from the coseismic deformation zone only derives from atmospheric noise and/or topographic errors. Therefore, we consider such noise as second-order stationary and use an exponential distance-dependent decay to build the covariance matrix $\boldsymbol{C}_d$ (Fig. S5; Sudhaus & Jónsson 2009; Jolivet *et al.* 2012). We build the prediction error matrix $\boldsymbol{C}_p$ according to the approach developed by Duputel *et al.* (2014) to include a 20 per cent uncertainty in our stratified elastic structure for the upper crust.

We downsample the InSAR coseismic displacement to 580 points for the ascending track and 630 points for the descending track using a quadtree approach to optimize the final resolution on the fault plane (Lohman & Simons 2005). Furthermore, we exclude data points located within 1 km of the fault to account for uncertainties related to the exact location of the fault trace. We use the AlTar2 software (https://github.com/AlTarFramework/altar, Minson *et al.* 2013; Jolivet *et al.* 2015), specifically designed to address high-dimensional problems, to derive the posterior PDF of our coseismic slip model. In comparison to traditional linear inversion methods, AlTar2 does not impose any form of prior regularization (i.e. smoothing) other than the choice of the geometry of the fault and its discretization. We run AlTar2 to draw 90 000 samples from the posterior PDF and explore such set of samples in the following.

3 FINITE-FAULT SLIP INVERSION

The optimal source within a homogeneous elastic half-space, shown in Table S2 and Fig. 2, has a strike of 26° and a dip angle of 73° to the east. Using such geometry, we show the strike-slip and dip-slip components of the mean of the *a posteriori* PDF (Figs 3 and S6). The 2023 Sarez earthquake ruptured two asperities, which did not reach the surface. Most of coseismic slip is indeed confined between ∼5 and 20 km depth, with a maximum strike-slip of

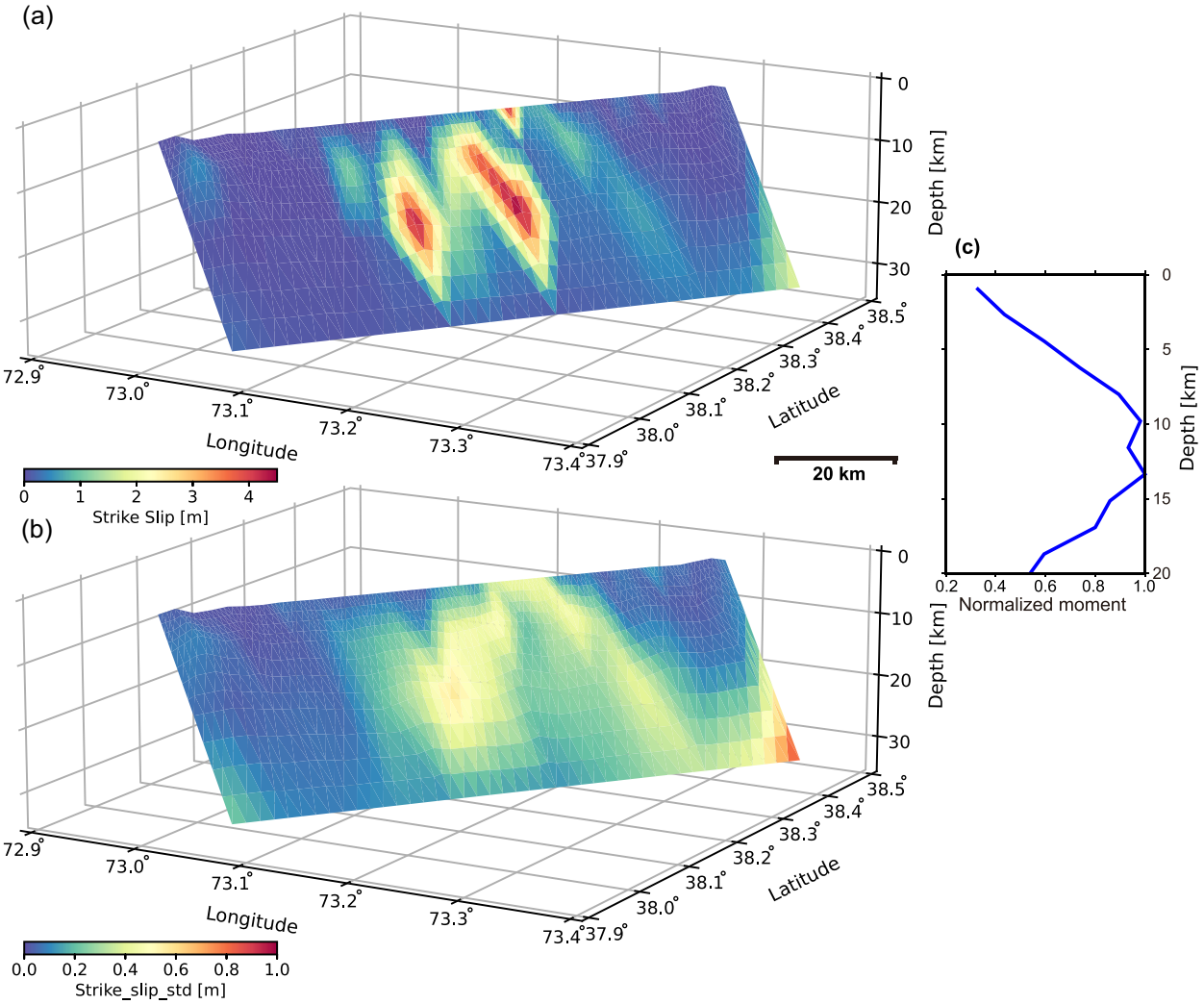

Figure 3. Mean coseismic slip model and associated uncertainties for the 2023 M_w 6.9 Sarez earthquake. (a) Mean slip distribution for the strike-slip component. (b) Standard deviation of the strike-slip component. (c) Variation of the normalized moment versus depth (Text S2 and Fig. S11 for computing details).

4.13 ± 0.33 m at 13 km-depth. Using a shear modulus of 31 GPa derived from the upper crust model (Fig. S4), the corresponding seismic moment is 2.71×10^{19} N · m for the strike-slip component and 2.25×10^{17} N · m for the dip-slip component, respectively. Comparing the moments released from dip-slip and strike-slip components, we confirm that the 2023 Sarez earthquake is predominantly a pure strike-slip earthquake, comparable to the focal mechanism of the 2015 Murghab earthquake 30 km to the west (Sangha *et al.* 2017).

The root mean square (RMS) of residual displacements is of 1.66 cm for the ascending track data and 1.32 cm for the ascending track (Fig. 4). *A posteriori* uncertainties on slip are lower than 1 m, suggesting a relatively well constrained slip model that fits the InSAR observations well (Fig. 3b). Minor local residuals near the fault trace might be attributed to inelastic deformation, more complex geometry of the seismogenic fault (Fig. 4). We also note that surface slip amounts for only 32 per cent of the peak slip at depth, indicating a significant shallow slip deficit (Fig. 3c).

4 POST-SEISMIC DEFORMATION MODELLING

As mentioned by Section 2.1, we use cross-fault short profiles to evaluate the amount of surface afterslip in the weeks following the main shock. Fig. 5a shows the location of 30 profiles (16 km-long, 2 km-wide) across the main shock fault trace. We then extract the LOS displacement (y) as a function of distance (x) to the fault trace along each profile (Fig. S7; Segall 2010):

$$y = \frac{-s}{\pi} \times \left[\arctan\left(\frac{x-l}{d}\right) - \frac{\pi}{2} \times sgn\,(x-l) \right] + o \qquad (2)$$

where s is the corresponding surface afterslip, d represents the depth of shallow dislocation, l (horizonal shift) and o (reference) are two constants. We estimate the best-fitting parameters using a least squares approach.

Ground motion mostly concentrates near the fault, decays rapidly, and becomes undetectable about 4 months after the main shock, suggesting ground motion mostly results from shallow afterslip (Fig. 5). We infer a maximum LOS offset of 2.71 ± 0.54 cm within one month after the 2023 Sarez earthquake (Figs 5b and S7). The majority of the post-seismic deformation occurs within the first month (Figs 5c–f). To further quantify the distribution of afterslip at depth, we solve for the distribution of strike-slip using the cumulative post-seismic displacement of the first month on the same fault plane as the coseismic model. We use the same method as for the coseismic slip distribution. Here, we keep the pixels located within 30 km of the fault trace as input for the inversion and constrain slip

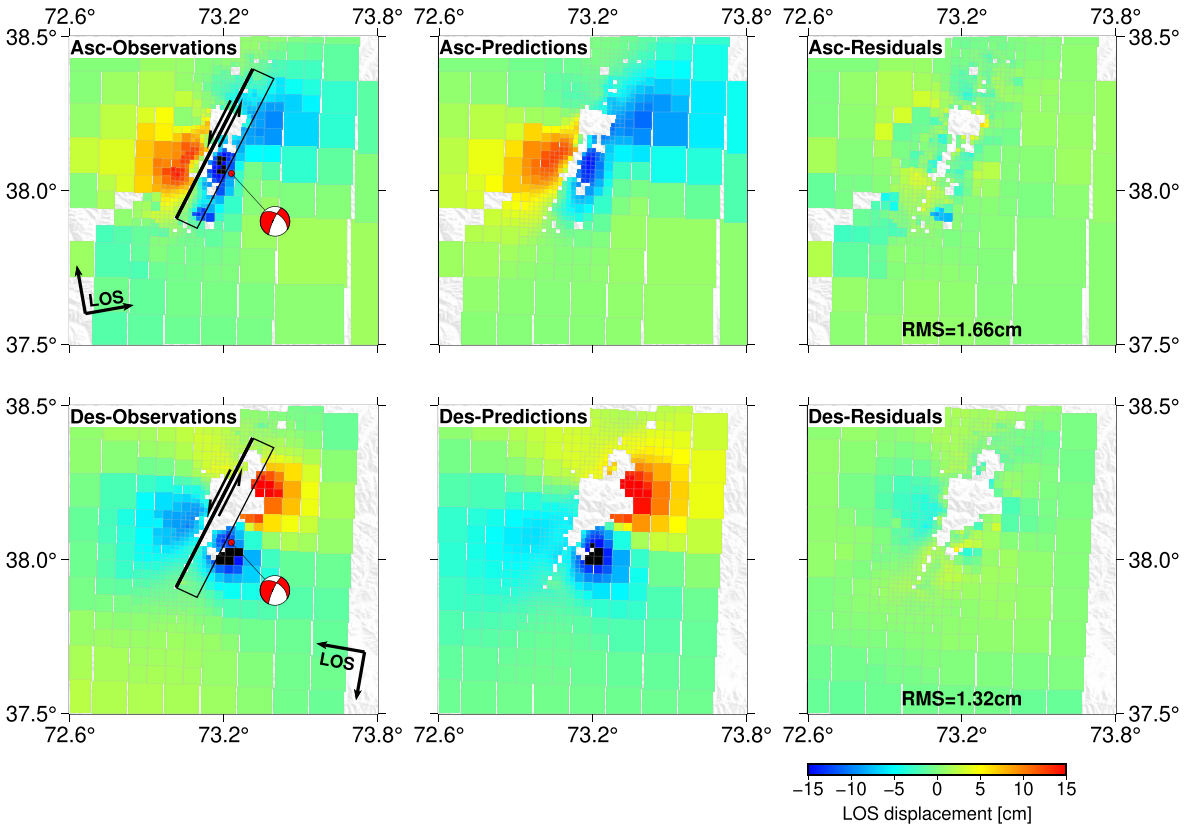

Figure 4. Comparisons of observed and modelled coseismic LOS displacements for both ascending and descending tracks. Black rectangle in ascending and descending observations represents the seismogenic fault with the bold line indicating the upper edge.

to be purely left-lateral. Fig. 6 shows the kinematic afterslip distribution. The corresponding LOS observations, model predictions, and residuals are shown in Fig. 7. We observe that only the largest asperity that ruptured coseismically leads to some afterslip with a maximum slip of 0.22 ± 0.04 m at a depth of 7 km (Fig. 6a). Compared to the coseismic slip distribution inferred previously, such afterslip does not catch up for all the shallow slip deficit. Finally, we observe that afterslip overlaps partially with the coseismic asperities. Although a rheological model would not be able to explain such feature (e.g. Perfettini *et al.* 2010), a moment conservation-based model would be a more plausible candidate here (Meade 2024).

5 DISCUSSION

5.1 Interaction between the 2015 Murghab and the 2023 Sarez earthquakes

The 2023 Sarez earthquake, 8 yr after the 2015 Murghab earthquake, also ruptured the SK fault system but on a different fault. It is, hence, tempting to investigate a potential triggering relationship between the 2015 event and the 2023 Sarez earthquake. We use the coseismic slip model of the 2015 Murghab earthquake from Jin *et al.* (2022) to evaluate the change in static stress imposed on the fault that ruptured in 2023 (Fig. S8). We compute the Coulomb stress change induced by the 2015 event to investigate whether the fault segment that hosted the 2023 event was brought closer to or away from failure (see Text S1 for modelling details). The distribution of static (coseismic) Coulomb stress changes induced by the 2015 event indicates the 2023 main shock fault is located within a positive Coulomb stress region (Figs 8 and S9, $\Delta CFS > 0.04$ MPa). We therefore conclude that the occurrence of the 2015 earthquake promoted failure of the 2023 earthquake, potentially advancing the clock on the rupture time for this event.

5.2 Characteristics of the finite-fault model

The geometry of preferred finite-fault model is consistent with previous studies which are used the linear inversion methods (e.g. Shi *et al.* 2023; Liu *et al.* 2024). Based on the same Sentinel-1A data, all studies identify a purely left-lateral strike-slip mechanism for the 2023 Sarez earthquake. However, the peak slip of our model is greater than that reported in previous studies (e.g. Shi *et al.* 2023; Liu *et al.* 2024), which obtained the distribution of fault slip using optimization-based inversion methods with regularization. Such discrepancies may derive from smoothing and regularization of the inverse problem. In the Bayesian inversion framework, we only set a reasonable range for the slip values based on knowledge about the physics of the problem without other constraints (see Minson *et al.* 2013, for more details). For example, in our case, we assume *a priori* that the largest coseismic slip cannot exceed 10 m, an upper bound high enough to allow a good parameter search for a M_w 6.9 earthquake. Our preferred slip model shown in Fig. 3(a) is the mean of the 90 000 samples drawn from the posterior PDF, and the corresponding standard deviation for all patches is less than 0.8 m (Fig. 3b). If our InSAR data were not constraining the finite-fault model in places, we would observe much larger standard deviation and a posterior distribution of slip that would be comparable to the

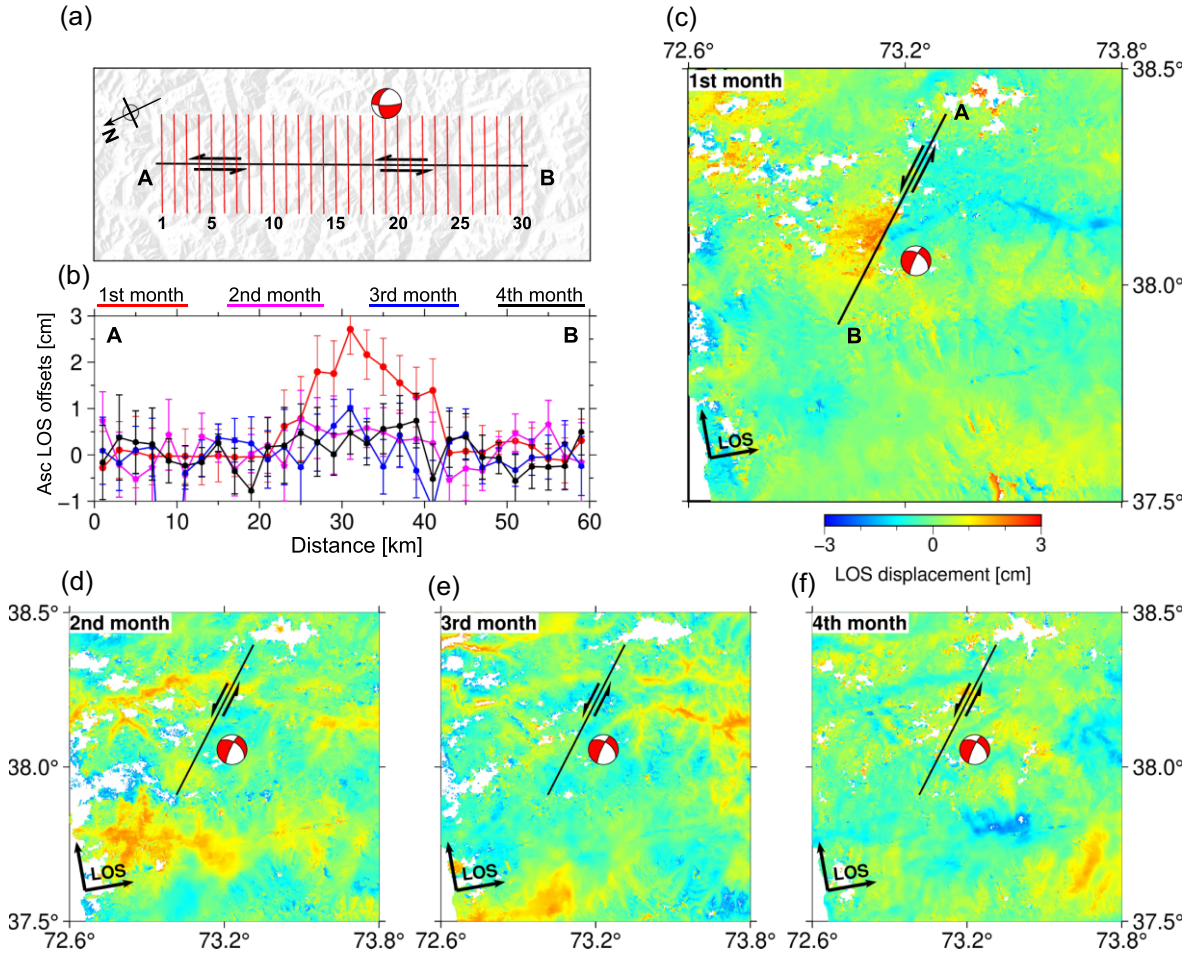

Figure 5. Early post-seismic deformation of the 2023 M_w 6.9 Sarez earthquake. (a) Location of 30 profiles across the main shock fault. (b) LOS offsets for each cross-fault profile in (a) were calculated from different ascending individual interferograms using eq. (2). Different colour lines represent the cumulative displacement for each month within the initial four months. Error bars denote 1σ variations. (c–f) Ground deformation of the coseismic area from the first month to the fourth month following the main shock derived from the ascending track. Black line represents the surface trace of the seismogenic fault. The red focal mechanism of the 2023 Sarez earthquake is from USGS.

prior PDF, which is not the case (Gombert *et al.* 2018). We therefore believe our model is robust and in particular considering the presence of a significant shallow slip deficit.

Intriguingly, the 2023 Sarez earthquake ruptured two adjacent asperities and the distribution of uncertainties suggest this feature is also robust (Fig. 3a). Earlier studies suggest various factors can influence the characteristics of earthquake rupture, including the geometrical complexities of the fault systems (e.g. Wesnousky 2006, 2008; Klinger 2010; Perrin *et al.* 2016; Hamling *et al.* 2017; Scognamiglio *et al.* 2018), along strike variations in frictional properties of the fault plane (i.e. with a rate-strengthening barrier, for instance, Kaneko *et al.* 2010) and variations in pre-stress (e.g. Kyriakopoulos *et al.* 2021; Chen *et al.* 2024b). In our case, the limited available data do not allow to refine the fault geometry and to relocate the aftershocks. We therefore cannot conclude which reason may explain such rupture pattern.

5.3 Shallow slip deficit

The coseismic slip model reveals a significant shallow slip deficit of 68 per cent (Fig. 3c). Compared to the coseismic slip zone, the afterslip migrates to shallower depth, with a maximum slip of 0.22 ± 0.04 m at a depth of 7 km. At the same depth, the coseismic slip is 2.15 ± 0.46 m, indicating that the magnitude of afterslip accounts for only ∼11 per cent of the shallow slip deficit. This suggests that the magnitude of afterslip is insufficient to compensate for all the shallow slip deficit caused by the coseismic rupture. Shallow slip deficit has been observed now in multiple cases and may arise from both technical limitations or be a real feature indicative of the rheology of the shallow crust (Fialko *et al.* 2005). From a technical perspective, decorrelation in near-field InSAR data, coarse patches at shallow depth, and smoothing of slip models would all result in a spurious shallow slip deficit (Milliner *et al.* 2015; Xu *et al.* 2016; Huang *et al.* 2017; Marchandon *et al.* 2021; Ma *et al.* 2024). In our study, we construct a finite-fault model using small patches at shallow depths and use an unregularized Bayesian sampling approach. Our preferred slip model shows the corresponding standard deviation associated with these shallow slip patches is less than 0.6 m (Fig. 3b), indicating the occurrence of shallow slip deficit in our model is robust. From a data point of view, we observe that maximum coseismic LOS displacements are not near the surface trace of the fault but rather away from it, suggesting the rupture of this earthquake predominantly involves

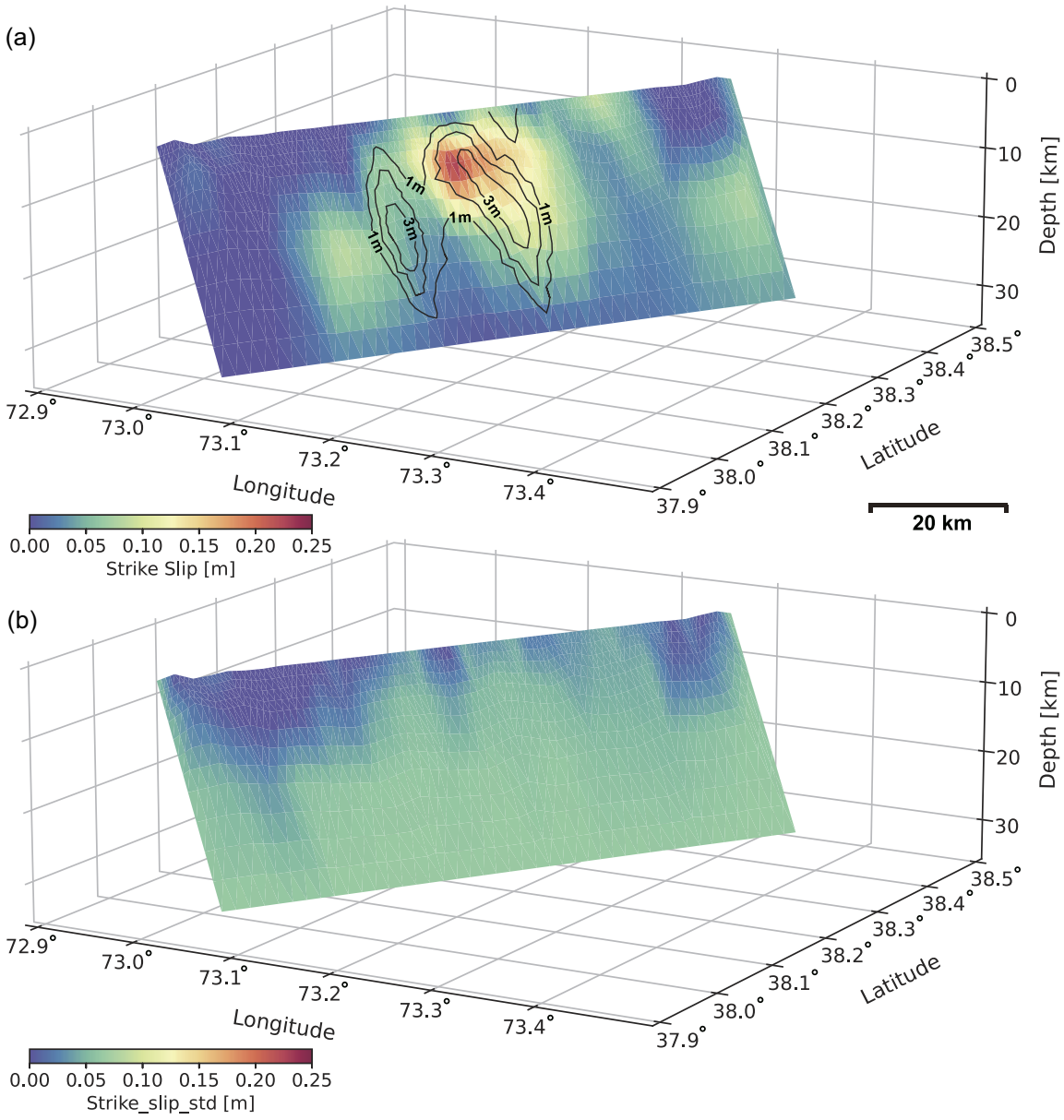

Figure 6. Kinematic afterslip model for the 2023 M_w 6.9 Sarez earthquake. (a) Mean slip distribution of the afterslip model. Black curves represent the contours of the coseismic slip. (b) Uncertainties of the afterslip model.

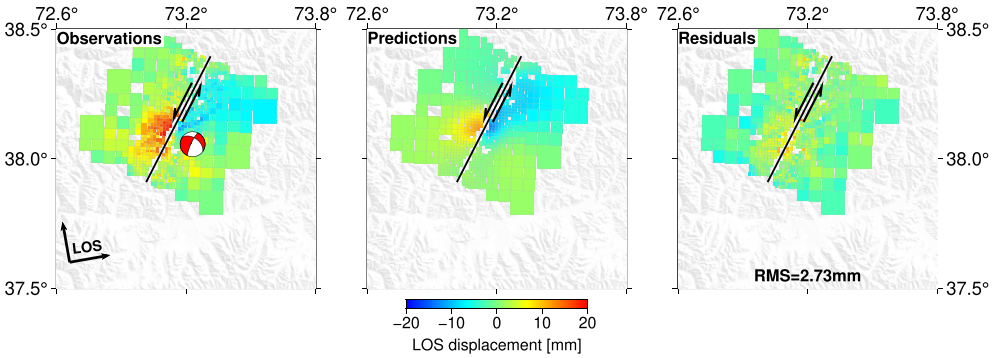

Figure 7. Comparison of the observed and modelled post-seismic LOS displacements for ascending track. Here, we retain the pixels located within 30 km of the main shock fault trace.

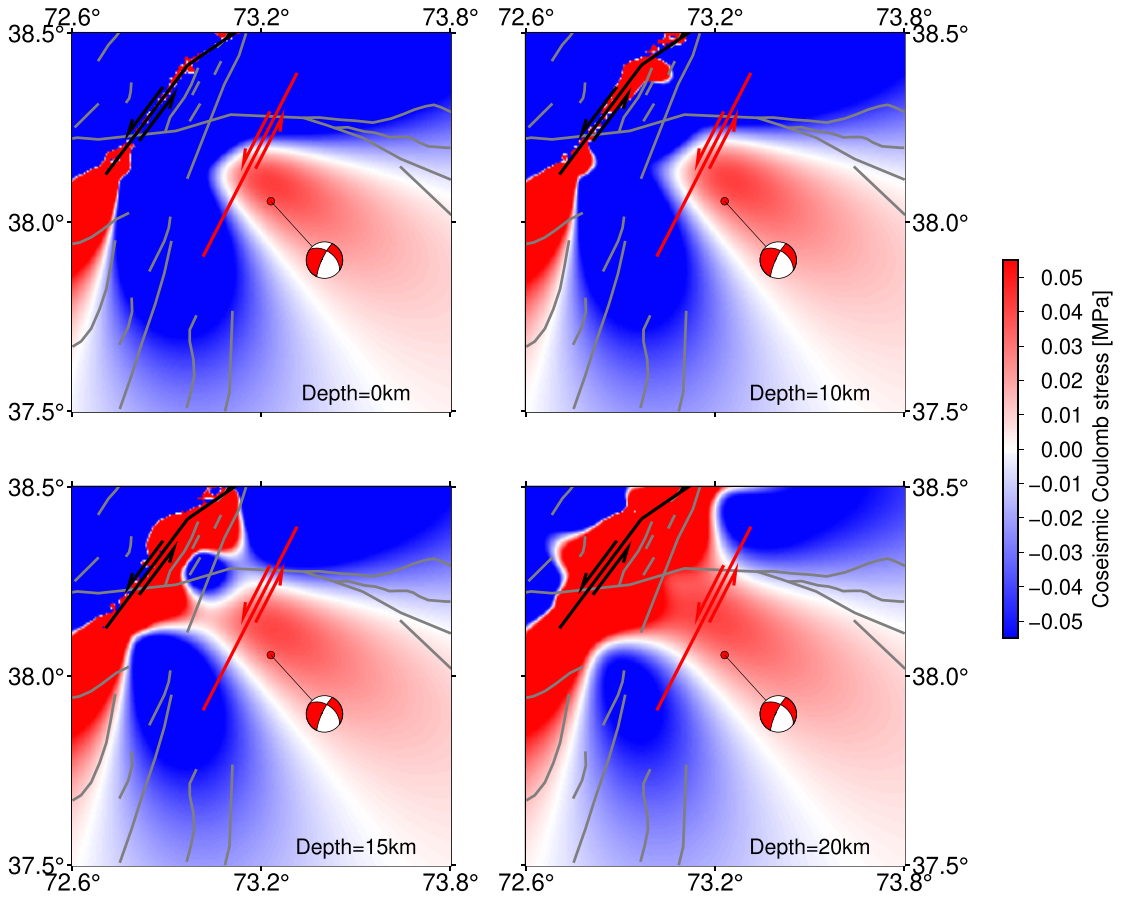

Figure 8. Spatial distribution of the coseismic Coulomb stress changes produced by the 2015 M_w 7.2 Murghab earthquake at different depths. The effective coefficient of friction is 0.4 (King *et al.* 1994; Tembe *et al.* 2006). Grey lines denote active faults in the central Pamir. Bold black line is the geometry of seismogenic fault of the 2015 M_w 7.2 Murghab earthquake (Jin *et al.* 2022). Red line indicates surface trace of the seismogenic fault of the 2023 M_w 6.9 Sarez earthquake determined by this study.

slip at depth (Figs 1c and d). From a physical perspective, shallow slip deficit may be compensated for through persistent shallow creep during the interseismic period or through other phases of the earthquake cycle to maintain the conservation of the long-term slip (Tse & Rice 1986). According to our post-seismic observations, no obvious aseismic slip surrounding the epicentre region after the first month has been observed, hence ruling out the possibility of detectable secular creep along the seismogenic fault. Longer time geodetic observations are needed to quantify the presence of potential interseismic slip, though.

Alternatively, field observations suggest that the shallow slip deficit may correlate with the structural maturity of a fault (Dolan & Haravitch 2014). With maturity defined as the total geological slip of a fault, earthquakes occurring on immature faults (i.e. less than 25 km of total offset) would exhibit much smaller normalized slip at the surface (<60 per cent) than those on mature faults (>85 per cent, Dolan & Haravitch 2014). This is thought to indicate that immature faults tend to produce more distributed deformation in the uppermost zone during coseismic rupture (e.g. Dixon & Xie 2018; Sadeghi Chorsi *et al.* 2022). Notably, a recent study suggests that shallow slip deficit is correlated with moment magnitude ($M_w > 6.4$), but not with cumulative offset (i.e. maturity; Sethanant *et al.* 2023). The 2023 M_w 6.9 Sarez earthquake exhibits significant shallow slip deficit and minor post-seismic deformation. Such patterns of coseismic deformation resulting from slip on immature faults have been documented after several major strike-slip earthquakes, including the 1992 M_w 7.3 Landers earthquake (Milliner *et al.* 2015), the 2003 M_w 6.5 Bam earthquake (Fialko et al 2005), the 2020 M_w 6.8 Elazığ earthquake (Pousse-Beltran *et al.* 2020) and the 2020 M_w 6.5 Nevada earthquake (Sadeghi Chorsi *et al.* 2022). Similarly, we speculate that the fault hosted the 2023 earthquake might have low structural maturity. However, detailed field investigations of active faulting and palaeoseismic ruptures are essential.

5.4 Deformation patten of the central Pamir

The 2023 earthquake, along with the dense seismicity detected by previous studies (Figs 1 and S10; Sippl *et al.* 2013; Schurr *et al.* 2014; Bloch *et al.* 2021, 2023), offers us valuable insight into the distribution of strain within the Pamir Plateau. The active SK fault system has ruptured twice within a short period of 8 yr. Distinct locations of the three major earthquakes rule out the possibility of repeating events, but rather indicate the rupture of parallel subfaults. Besides, minimal post-seismic deformation was observed for the 2015 Murghab earthquake and the 2023 Sarez earthquake. Both earthquakes are located at the southern end of the SK fault system, which itself might be at an incipient stage of development, slowly moving through a distributed deformation

zone (Schurr *et al.* 2014; Jin *et al.* 2022). Furthermore, as seen from the limited earthquake catalogue in this region, strike-slip earthquakes do not seem to align along the SK fault system but are rather scattered within the eastern and western Pamir (Fig. 1a; Schurr *et al.* 2014). Although such distributed seismicity should be validated by additional data, our results and previous studies indicate that north–south shear strain across the central Pamir is mainly partitioned on a series of subparallel faults, resulting in intensive earthquakes with similar focal mechanisms within this region. Such inference may explain why three major strike-slip earthquakes occurred in the region within only a short period of 100 yr.

6 CONCLUSION

We investigate the coseismic and early post-seismic deformation of the 2023 M_w 6.9 Sarez earthquake that occurred in the central Pamir using Sentinel-1A InSAR data. Based on the LOS coseismic displacement, we characterize the seismogenic fault geometry and slip distribution. Our results indicate an NNE fault with a strike of 26° that gently dips to the southeast with a dip angle of 73°. The coseismic rupture is predominantly purely strike-slip with a maximum slip of 4.13 ± 0.33 m at a depth of 13 km. Considering that post-seismic deformation following this event decays rapidly and disappears after the first month, the shallow slip deficit exhibited by the coseismic slip distribution is not fully compensated for, implying a potentially lower structural maturity for the seismogenic fault. We interpret the occurrence of such an earthquake on a potentially immature fault, together with the nearby 2015 and 1911 earthquakes, as the signature of the broadly distributed termination of the SK fault zone, potentially progressing southward, accommodating the asymmetric motion of the Pamir northward.

ACKNOWLEDGMENTS

The authors express thanks to Zeyu Jin for sharing the coseismic slip model of the 2015 M_w 7.2 Murghab earthquake. This work is supported by the National Natural Science Foundation of China (Grants U2139202, 42374005). Romain Jolivet acknowledges funding from the Institut Universitaire de France. This work has also received funding from the European Research Council (ERC) under the European Union's Horizon 2020 research and innovation program (Grant 758210 for project Geo4D). Funding to Bryan Raimbault is supported by MIAI@Grenoble Alpes (Grant ANR-19-P3IA-0003). Xing Huang acknowledges funding from the State Scholarship Fund of China Scholarship Council (Grant No. 202104190004). We also thank the Editor, Kosuke Heki, for handling our paper, and reviewer Zhangfeng Ma and an anonymous reviewer for their valuable comments.

AUTHOR CONTRIBUTIONS

Xing Huang (conceptualization, data curation, investigation, validation, writing-original draft, visualization), Romain Jolivet (software, methodology, writing-review and editing, validation, Funding acquisition, supervision), Yanchuan Li (conceptualization, writing-review and editing, validation, Funding acquisition), Xinjian Shan (writing-review and editing, validation, Funding acquisition, supervision) and Bryan Raimbault (software, writing-review and editing, validation, Funding acquisition)

SUPPORTING INFORMATION

Supplementary data are available at *GJI* online.

Figure S1. Coseismic interferograms for the 2023 M_w 6.9 Sarez earthquake from the ascending track. Because of much atmospheric phase delay influencing the ascending images, we enlarged the temporal baselines and processed six interferograms (Table S1). The interferogram (20230122-20230311) has better coherence than others.

Figure S2. Corrections of coseismic deformation associated with the 2023 M_w 6.9 Sarez earthquake derived from ascending and descending tracks. (a) and (e) Unwrapped LOS displacements. (b) and (f) GACOS tropospheric delay predictions in LOS direction. (c) and (g) Inferred ramp in LOS direction. (d) and (h) Coseismic interferograms after corrections.

Figure S3. 3-D (a) and 2-D (b) views of the finite-fault model for the 2023 M_w 6.9 Sarez earthquake.

Figure S4. Coarse structure of the elastic crust in the central Pamir. V_s and V_p represent the velocities of S and P waves, respectively. The stratified crust model and waves velocities are from Mechie *et al.* (2012). ρ is the rock density from Crust 1.0 (Laske *et al.* 2013).

Figure S5. Empirical covariance functions for the ascending and descending coseismic deformation maps, for which the approach is described in Jolivet *et al.* (2012): $C_{i,j} = \sigma^2 e^{-\frac{\|i,j\|^2}{\lambda}}$. Dots are the empirical covariances. Curves represent the exponential fit to the covariance functions.

Figure S6. Average coseismic dip-slip model and associated uncertainties for the 2023 M_w 6.9 Sarez earthquake. (a) Average slip distribution for the dip-slip component. (b) Standard deviation of the dip-slip component.

Figure S7. LOS afterslip of the interferogram (20230227–20230323) along the seismogenic fault trace. Grey points represent the InSAR points. We fit profile boxes using the function $y = \frac{-s}{\pi} \times [\arctan\left(\frac{x-l}{d}\right) - \frac{\pi}{2} \times \mathrm{sgn}(x-l)] + o$. In this study, we only consider the value of S, which indicates fault offset in the direction of LOS. Red line in each subgraph shows the best-fitting model. The same method is used in other interferograms to calculate the offsets across the fault (Fig. 5b).

Figure S8. Coseismic slip model of the 2015 M_w 7.2 Murghab earthquake (Jin *et al.* 2022).

Figure S9. Spatial distribution of the coseismic Coulomb stress changes produced by the 2015 M_w 7.2 Murghab earthquake with different effective coefficients of friction at the same depth. The computation depth is 13 km corresponding to the hypocentre depth of the 2023 Sarez earthquake. The top-left-hand panel shows the projection of the coseismic slip model of the 2023 Sarez earthquake in the plane. The rest of caption is the same as in Fig. 8.

Figure S10. Microseismic distribution in the central Pamir. Blue dots represent the seismicity measured from August 2008 to July 2010 (Sippl *et al.* 2013). Orange dots represent the seismicity measured from August 2015 to December 2015 (Bloch *et al.* 2023). Bold black line denotes the geometry of seismogenic fault of the 2015 M_w 7.2 Murghab earthquake (Jin *et al.* 2022). Red line is surface trace of seismogenic fault of the 2023 M_w 6.9 Sarez earthquake determined by this study.

Figure S11. Average coseismic strike-slip distribution (Fig. 3a) interpolated on a series of subrectangular faults characterized by a length of 2 km and a width of 2 km.

Table S1. Interferograms for coseismic and post-seismic deformation of the 2023 M_w 6.9 Sarez earthquake. Bold fonts indicate the interferogram has been used in our analysis.
Table S2. Priors and optimal source parameters for the 2023 M_w 6.9 Sarez earthquake.

Please note: Oxford University Press is not responsible for the content or functionality of any supporting materials supplied by the authors. Any queries (other than missing material) should be directed to the corresponding author for the paper.

CONFLICTS OF INTEREST

The authors declare that they have no competing interests.

DATA AVAILABILITY

The Sentinel-1 images used in this study are provided by the European Space Agency and available through the Alaska Satellite Facility (https://www.asf.alaska.edu/#/). All data used in the inversions can be accessed by contacting the corresponding author.

REFERENCES

Bagnardi,, M. & Hooper,, A. 2018. Inversion of surface deformation data for rapid estimates of source parameters and uncertainties: a Bayesianapproach, *Geochem. Geophys. Geosyst.,* **19**(7), 2194–2211.

Bloch, W., *et al.*, 2021. Structure and stress field of the lithosphere between Pamir and Tarim, *Geophys. Res. Lett.,* **48**(22), e2021GL095413, doi: 10.1029/2021GL095413.

Bloch, W., *et al.*, 2023. The 2015-2017 Pamir earthquake sequence: foreshocks, main shocks and aftershocks, seismotectonics, fault interaction and fluid processes, *Geophys. J. Int.,* **233**(1), 641–662.

Burtman, V.S. & Molnar, P., 1993. Geological and geophysical evidence for deep subduction of continental crust beneath the Pamir, *Spec. Paper Geol. Soc. Am.,* **281,** 1–76.

Chen, C. & Zebker, H., 2002. Phase unwrapping for large SAR interferograms: statistical segmentation and generalized network models, *IEEE Trans. Geosci. Remote Sens.,* **40**(8), 1709–1719.

Chen, F., *et al.*, 2024a. Mechanism and implications of the post-seismic deformation following the 2021 M w 7.4 Maduo (Tibet) earthquake, *Geophys. J. Int.,* **237**(1), 203–216.

Chen, K., *et al.*, 2024b. Super-shear ruptures steered by pre-stress heterogeneities during the 2023 Kahramanmaraş earthquake doublet, *Nat. Commun.,* **15**(1), 7004, doi: 10.1038/s41467-024-51446-y.

Cowgill, E., 2010. Cenozoic right-slip faulting along the eastern margin of the Pamir salient, northwestern China, *Geol. Soc. Am. Bull.,* **122**(1-2), 145–161.

Dixon, T.H. & Xie, S., 2018. A kinematic model for the evolution of the eastern California shear zone and Garlock fault, Mojave Desert, California, *Earth planet. Sci. Lett.,* **494,** 60–68.

Dolan, J.F. & Haravitch, B.D., 2014. How well do surface slip measurements track slip at depth in large strike-slip earthquakes? The importance of fault structural maturity in controlling on-fault slip versus off-fault surface deformation, *Earth planet. Sci. Lett.,* **388,** 38–47.

Duputel, Z., Agram, P.S., Simons, M., Minson, S.E. & Beck, J.L., 2014. Accounting for prediction uncertainty when inferring subsurface fault slip, *Geophys. J. Int.,* **197**(1), 464–482.

Elliott, A., Elliott, J., Hollingsworth, J., Kulikova, G., Parsons, B. & Walker, R., 2020. Satellite imaging of the 2015 M 7.2 earthquake in the Central Pamir, Tajikistan, elucidates a sequence of shallow strike-slip ruptures of the Sarez-Karakul fault, *Geophys. J. Int.,* **221**(3), 1696–1718.

Farr, T.G., *et al.*, 2007. The Shuttle radar topography mission, *Rev. Geophys.,* **45**(2), doi:10.1029/2005RG000183.

Fialko, Y., Sandwell, D., Simons, M. & Rosen, P., 2005. Three-dimensional deformation caused by the Bam, Iran, earthquake and the origin of shallow slip deficit, *Nature,* **435**(7040), 295–299.

Gombert, B., Duputel, Z., Jolivet, R., Doubre, C., Rivera, L. & Simons, M., 2018. Revisiting the 1992 Landers earthquake: a Bayesian exploration of co-seismic slip and off-fault damage, *Geophys. J. Int.,* **212**(2), 839–852.

Hamling, I.J., *et al.*, 2017. Complex multifault rupture during the 2016 Mw 7.8 Kaikoura earthquake, New Zealand, *Science,* **356**(6334), doi:10.1126/science.aam7194.

Huang, M.H., Fielding, E.J., Dickinson, H., Sun, J., Gonzalez-Ortega, J.A., Freed, A.M. & Bürgmann, R., 2017. Fault geometry inversion and slip distribution of the 2010 Mw 7.2 El Mayor-Cucapah earthquake from geodetic data, *J. geophys. Res.,* **122**(1), 607–621.

Ischuk, A., *et al.*, 2013. Kinematics of the Pamir and Hindu Kush regions from GPS geodesy, *J. geophys. Res.,* **118**(5), 2408–2416.

Jin, Z., Fialko, Y., Zubovich, A. & Schöne, T., 2022. Lithospheric deformation due to the 2015 M7.2 Sarez (Pamir) earthquake constrained by 5 years of space geodetic observations, *J. geophys. Res.,* **127**(4), e2021JB022461, doi: 10.1029/2021JB022461.

Jolivet, R., *et al.*, 2012. Shallow creep on the Haiyuan Fault (Gansu, China) revealed by SAR Interferometry, *J. geophys. Res.,* **117**(B6), doi:10.1029/2011JB008732.

Jolivet, R., *et al.*, 2014. The 2013 Mw 7.7 Balochistan earthquake: seismic potential of an accretionary wedge, *Bull. seism. Soc. Am.,* **104**(2), 1020–1030.

Jolivet, R., *et al.*, 2023. Daily to centennial behavior of aseismic slip along the central section of the North Anatolian Fault, *J. geophys. Res.,* **128**(7), e2022JB026018, doi: 10.1029/2022JB026018.

Jolivet, R., Simons, M., Agram, P.S., Duputel, Z. & Shen, Z.-K., 2015. Aseismic slip and seismogenic coupling along the central San Andreas Fault, *Geophys. Res. Lett.,* **42**(2), 297–306.

Jolivet, R., Simons, M., Duputel, Z., Olive, J.-A., Bhat, H.S. & Bletery, Q., 2020. Interseismic loading of subduction megathrust drives long-term uplift in Northern Chile, *Geophys. Res. Lett.,* **47**(8), e2019GL08537, doi: 10.1029/2019GL085377.

Kaneko, Y., Avouac, J.P. & Lapusta, N., 2010. Towards inferring earthquake patterns from geodetic observations of interseismic coupling, *Nat. Geosci.,* **3**(5), 363–369.

King, G.C.P., Stein, R.S. & Lin, J., 1994. Static stress changes and the triggering of earthquakes, *Bull. Seismol. Soc. Am.,* **84**(3), 935–953.

Klinger, Y., 2010. Relation between continental strike-slip earthquake segmentation and thickness of the crust, *J. Geophys. Res.,* **115**(B7), B07306.

Kulikova, G., Schurr, B., Krüger, F., Brzoska, E. & Heimann, S., 2016. Source parameters of the Sarez-Pamir earthquake of 1911 February 18, *Geophys. J. Int.,* **205**(2), 1086–1098.

Kyriakopoulos, C., Wu, B. & Oglesby, D.D., 2021. Asymmetric topography causes normal stress perturbations at the rupture front: the case of the Cajon pass, *Geophys. Res. Lett.,* **48**(20), e2021GL095397, doi: 10.1029/2021GL095397.

Laske, G., *et al.*, 2013. Update on CRUST1.0–A 1–degree Global Model of Earth's Crust, *Geophysical Research Abstracts,* **15,** EGU2013–2658.

Liu, Z., *et al.*, 2024. Stress triggering and future seismic hazards implied by four large earthquakes in the Pamir from 2015 to 2023 revealed by Sentinel-1 radar interferometry, *Geophys. J. Int.,* **237,** 887–901.

Lohman, R.B. & Simons, M., 2005. Some thoughts on the use of InSAR data to constrain models of surface deformation: noise structure and data downsampling, *Geochem. Geophys. Geosyst.,* **6**(1), doi:10.1029/2004GC000841.

Ma, Z., *et al.*, 2024. Space geodetic insights to the dramatic stress rotation induced by the February 2023 Turkey-Syria earthquake doublet, *Geophys. Res. Lett.,* **51,** e2023GL107788, doi: 10.1029/2023GL107788.

Marchandon, M., Hollingsworth, J. & Radiguet, M., 2021. Origin of the shallow slip deficit on a strike slip fault: influence of elastic structure, topography, data coverage, and noise, *Earth planet. Sci. Lett.,* **554,** doi:10.1016/j.epsl.2020.116696.

Meade, B.J., 2024. Kinematic afterslip patterns, *Geophys. Res. Lett.,* **51**(1), e2023GL105797.

Mechie, J., Yuan, X., Schurr, B., Schneider, F., Sippl, C., Ratschbacher, L. *et al.*, 2012. Crustal and uppermost mantle velocity structure along a profile across the Pamir and southern Tien Shan as derived from project TIPAGE wide-angle seismic data, *Geophys. J. Int.,* **188**(2), 385–407.

Milliner, C.W.D., Dolan, J.F., Hollingsworth, J., Leprince, S., Ayoub, F. & Sammis, C.G., 2015. Quantifying near-field and off-fault deformation patterns of the 1992 Mw 7.3 Landers earthquake, *Geochem. Geophys. Geosyst.,* **16**(5), 1577–1598.

Minson, S.E., Simons, M. & Beck, J.L., 2013. Bayesian inversion for finite fault earthquake source models I-theory and algorithm, *Geophys. J. Int.,* **194**(3), 1701–1726.

Mohadjer, S., *et al.*, 2010. Partitioning of India-Eurasia convergence in the Pamir-Hindu Kush from GPS measurements, *Geophys. Res. Lett.,* **37**(4), 1–6.

Okada, Y., 1985. Surface deformation due to shear and tensile faults in a half-space, *Bull. seism. Soc. Am.,* **75,** 1135–1154.

Perfettini, H., *et al.*, 2010. Seismic and aseismic slip on the Central Peru megathrust, *Nature,* **465**(7294), 78–81.

Perrin, C., Manighetti, I. & Gaudemer, Y., 2016. Off-fault tip splay networks: a genetic and generic property of faults indicative of their long-term propagation, *C.R. Geosci.,* **348**(1), 52–60.

Persson, P.-O. & Strang, G., 2004. A simple mesh generator in MATLAB, *SIAM Rev.,* **46**(2), 329–345.

Pousse-Beltran, L., Nissen, E., Bergman, E.A., Cambaz, M.D., Gaudreau, É., Karasözen, E. & Tan, F., 2020. The 2020 Mw 6.8 Elazığ (Turkey) earthquake reveals rupture behavior of the East Anatolian Fault, *Geophys. Res. Lett.,* **47**(13), e2020GL088136, doi: 10.1029/2020GL088136.

Rosen, P.A., Gurrola, E., Sacco, G.F. & Zebker, H., 2012. The InSAR scientific computing environment, in *EUSAR 2012: Proceedings of the 9th European Conference on Synthetic Aperture Radar,* 23–26 April 2012, Nuremberg, Germany, pp. 730–733.

Sadeghi Chorsi, T., Braunmiller, J., Deng, F. & Dixon, T.H., 2022. Afterslip from the 2020 M 6.5 Monte Cristo Range, Nevada earthquake, *Geophys. Res. Lett.,* **49**(17), e2022GL099952, doi: 10.1029/2022GL099952.

Sangha, S., Peltzer, G., Zhang, A., Meng, L., Liang, C., Lundgren, P. & Fielding, E., 2017. Fault geometry of 2015, Mw7.2 Murghab, Tajikistan earthquake controls rupture propagation: insights from InSAR and seismological data, *Earth planet. Sci. Lett.,* **462,** 132–141.

Schurr, B., Ratschbacher, L., Sippl, C., Gloaguen, R., Yuan, X. & Mechie, J., 2014. Seismotectonics of the Pamir, *Tectonics,* **33**(8), 1501–1518.

Schwab, M., *et al.*, 2004. Assembly of the Pamirs: age and origin of magmatic belts from the southern Tien Shan to the southern Pamirs and their elation to Tibet, *Tectonics,* **23**(4), doi:10.1029/2003TC001583.

Scognamiglio, L., *et al.*, 2018. Complex fault geometry and rupture dynamics of the Mw6.5, 30 October 2016, central Italy earthquake, *J. geophys. Res.,* **123,** 2943–2964.

Segall, P., 2010. *Earthquake and Volcano Deformation,* Princeton Univ. Press.

Sethanant, I., Nissen, E., Pousse-Beltran, L., Bergman, E. & Pierce, I., 2023. The 2020 Mw 6.5 Monte Cristo Range, Nevada, earthquake: anatomy of a crossing-fault rupture through a region of highly distributed deformation, *Bull. seism. Soc. Am.,* **113**(3), 948–975.

Shi, Y., Wang, Y. & Bian, Y., 2023. Coseismic source model of the February 2023 Mw 6.8 Tajikistan earthquake from sentinel-1A InSAR observations and its associated earthquake hazard, *Remote. Sens.,* **15**(12), 3010, doi: 10.3390/rs15123010.

Sippl, C., *et al.*, 2013. Geometry of the Pamir-Hindu Kush intermediate-depth earthquake zone from local seismic data, *J. geophys. Res.,* **118**(4), 1438–1457.

Sobel, E.R., Schoenbohm, L.M., Chen, J., Thiede, R., Stockli, D.F., Sudo, M. & Strecker, M.R., 2011. Late Miocene-pliocene deceleration of dextral slip between Pamir and Tarim: implications for Pamir orogenesis, *Earth planet. Sci. Lett.,* **304**(3-4), 369–378.

Sudhaus, H. & Jónsson, S., 2009. Improved source modelling through combined use of InSAR and GPS under consideration of correlated data errors: application to the June 2000 Kleifarvatn earthquake, Iceland, *Geophys. J. Int.,* **176**(2), 389–404.

Tapponnier, P., Mattauer, M., Proust, F. & Cassaigneau, C., 1981. Mesozoic ophiolites, sutures, and arge-scale tectonic movements in Afghanistan, *Earth planet. Sci. Lett.,* **52**(2), 355–371.

Tembe, S., Lockner, D.A., Solum, J.G., Morrow, C.A., Wong, T.-F. & Moore, D.E., 2006. Frictional strength of cuttings and core from safod drillhole phases 1 and 2, *Geophys. Res. Lett.,* **33**(23), 1–5.

Tse, S.T. & Rice, J.R., 1986. Crustal earthquake instability in relation to the depth variation of frictional slip properties, *J. geophys. Res.,* **91**(B9), 9452–9472.

USGS, 2023. U.S. Geological survey. *M*6.9-65 km WSW of Murghob, Tajikistan. Retrieved from: https://earthquake.usgs.gov/earthquakes/eventpage/us6000jqxc/executive.

Vajedian, S., Motagh, M., Wetzel, H.-U. & Teshebaeva, K., 2017. Coupling of Sentinel-1, Sentinel-2 and ALOS-2 to assess coseismic deformation and earthquake-induced landslides following the 26 June, 2016 earthquake in Kyrgyzstan, in *EGU2017: Proceedings of the 19th EGU General Assembly,* held 23–28 April 2017 in Vienna, Austria, p. 18464.

Wang, K. & Fialko, Y., 2015. Slip model of the 2015 Mw7.8 Gorkha (Nepal) earthquake from inversions of ALOS-2 and GPS data, *Geophys. Res. Lett.,* **42**(18), 7452–7458.

Wang, M. & Shen, Z.-K., 2020. Present-day crustal deformation of continental China derived from GPS and its tectonic implications, *J. geophys. Res.,* **125**(2), e2019JB018774, doi: 10.1029/2019JB018774.

Wesnousky, S.G., 2006. Predicting the endpoints of earthquake ruptures, *Nature,* **444**(7117), 358–360.

Wesnousky, S.G., 2008. Displacement and geometrical characteristics of earthquake surface ruptures: issues and implications for seismic hazard analysis and the process of earthquake rupture, *Bull. seism. Soc. Am.,* **98**(4), 1609–1632.

Xu, X., Tong, X., Sandwell, D.T., Milliner, C.W.D., Dolan, J.F., Hollingsworth, J., Leprince, S. & Ayoub, F., 2016. Refining the shallow slip deficit, *Geophys. J. Int.,* **204**(3), 1843–1862.

Yu, C., Li, Z. & Penna, N.T., 2018. Interferometric synthetic aperture radar atmospheric correction using a GPS-based iterative tropospheric decomposition model, *Remote Sens. Environ.,* **204,** 109–121.

Yu, C., Li, Z. & Penna, N.T., 2020. Triggered afterslip on the southern Hikurangi subduction interface following the 2016 Kaikōura earthquake from InSAR time series with atmospheric corrections, *Remote Sens. Environ.,* **251,** doi:10.1016/j.rse.2020.112097.

Yu, C., Penna, N.T. & Li, Z., 2017. Generation of real-time mode high resolution water vapor fields from GPS observations, *J. geophys. Res.,* **122**(3), 2008–2025.

Zhao, D., Qu, C., Chen, H., Shan, X., Song, X. & Gong, W., 2021. Tectonic and geometric control on fault kinematics of the 2021 Mw7.3 Maduo (China) earthquake inferred from interseismic, coseismic, and post-seismic InSAR observations, *Geophys. Res. Lett.,* **48**(18), e2021GL095417, doi: 10.1029/2021GL095417.

Zhu, L. & Rivera, L.A., 2002. A note on the dynamic and static displacements from a point source in multilayered media, *Geophys. J. Int.,* **148**(3), 619–627.

Zubovich, A.V., *et al.*, 2010. GPS velocity field for the Tien Shan and surrounding regions, *Tectonics,* **29**(6), doi:10.1029/2010TC002772.